

Anti-aggregation self-assembled monolayers enable high-performance and scalable perovskite solar cells

Received: 11 May 2025

Accepted: 22 December 2025

Published online: 08 January 2026

 Check for updates

Kaihuai Du¹, Chunna Huang¹, Aili Wang¹✉, Haoran Zhang¹, Lvzhou Li¹✉, Xu Dong¹, Luozheng Zhang¹✉, Mohammad Khaja Nazeeruddin^{2,3}✉, Guixiang Li⁴✉ & Jianning Ding^{1,5}✉

Stable self-assembled monolayers (SAMs), such as (2-(9H-carbazol-9-yl)) ethylphosphonic acid (2PACz), are crucial for reducing interfacial energy loss in high-performance perovskite solar cells (PSCs). However, the inherent aggregation tendency of SAMs at the buried interface hinders the device's performance. Here, we propose a surfactant-assisted strategy to inhibit the aggregation of 2PACz by functionalizing cetyltrimethylammonium bromide (CTAB). Capitalizing on its distinctive electrostatic potential distribution, CTAB engages in non-bonding interactions with 2PACz. Theoretical and experimental characterizations prove that this promotes the uniform dispersion and anchoring of 2PACz on the substrate, leading to the SAM formation with high surface potential and excellent coverage. Moreover, the perovskite films with CTAB-modified SAM exhibit enhanced crystallinity with reduced trap state density and improved hole extraction efficiency. Consequently, the PSCs with a p-i-n architecture achieve a power conversion efficiency (PCE) of 26.20% (0.072 cm²). Scaled-up modules attain a PCE of 22.34% (22.96 cm²), confirming the scalability. Additionally, anti-aggregation-SAMs-integrated devices demonstrate stability, maintaining over 80% and 90% of their initial PCEs after tracking at maximum power point for 800 h and ageing at 65 °C for 1000 h, respectively.

Perovskite solar cells (PSCs) have emerged as a revolutionary photovoltaic technology, with p-i-n structured devices achieving remarkable power conversion efficiencies (PCEs) exceeding 26%, primarily attributed to the strategic implementation of self-assembled monolayers (SAMs), such as (2-(9H-carbazol-9-yl)) ethylphosphonic acid (2PACz)^{1–6}. These SAMs effectively minimize interfacial energy losses while maintaining compatibility with scalable fabrication processes^{7–9}.

However, their inherent aggregation tendency on textured substrates, driven by strong intermolecular interactions and solvent-mediated effects during deposition, induces micelle formation and discontinuous surface coverage^{10–15}. This phenomenon generates nanoscale voids and high-resistance pathways that exacerbate interfacial defects and impede charge transport, thereby compromising both device performance and operational stability^{16–18}.

¹Institute of Technology for Carbon Neutralization, School of Physical Science and Technology, Yangzhou University, Yangzhou, Jiangsu, PR China. ²Institute of Chemical Sciences and Engineering, École Polytechnique Fédérale de Lausanne (EPFL), Lausanne, CH, Switzerland. ³School of Integrated Circuits, Southeast University, Wuxi, Jiangsu, PR China. ⁴School of Materials Science and Engineering, Southeast University, Nanjing, Jiangsu, PR China. ⁵Jiangsu Collaborative Innovation Center for Photovoltaic Science and Engineering, Jiangsu Province Cultivation Base for State Key Laboratory of Photovoltaic Science and Technology, Changzhou University, Changzhou, PR China. ✉e-mail: wangal@yzu.edu.cn; oasis@yzu.edu.cn; mdkhaja.nazeeruddin@epfl.ch; guixiang.li@seu.edu.cn; dingjn@yzu.edu.cn

To address the inherent aggregation and interfacial defects in SAMs deposition process, researchers employed conjugated organic molecules, polymers or cosolvent systems to weaken the SAMs micellization tendency and enable denser interface passivation^{19–23}. It was found that 3-mercaptopropionic acid (3-MPA) molecules, 6-aminohexane-1-sulfonic acid (SA) molecules, 4,4',4''-nitrotribenzoic acid (NA) molecules or diamide-terminated functionalized assembly molecules promoted SAMs to form a uniform and dense hole transport layer through covalent bond forces or co-assembly strategies^{23–25}. Additionally, Alex et al. destroyed the micelle structure of amphiphilic carbazole-based SAMs in alcohol solvents through a co-solvent strategy, increasing the critical micelle concentration and anchoring group reactivity, thereby forming dense SAMs²⁶. Conjugated organic molecules, polymers or solvents as dispersants can enhance the dispersibility or interfacial electrical properties of SAMs. However, such covalent coordination, inherent rigid bonding in self-assembled structure or solvent polarity changes, would cause competitive adsorption behavior, phase separation risk and imbalanced charge transfer, posing challenges to the precise regulation of SAMs. In contrast, non-self-assembled and non-conductive surfactants have the advantages of reducing surface tension, inhibiting particle agglomeration, and reducing the risk of phase separation, which can be used as an ideal candidate material for finely regulating the microstructure and properties of nanomaterials^{10,27}. However, there is still a lack of in-depth understanding of how to use them to overcome the thermodynamic limitations of strong intermolecular interactions and solvent-mediated assembly, especially in the application of complex texture substrates and submicron voids.

In this work, we adopt a non-self-assembled, non-conductive cationic surfactant, cetyltrimethylammonium bromide (CTAB) as a regulator to inhibit 2PACz aggregation. By leveraging its special electrostatic potential distribution (positively charged N atom), CTAB engage non-bonding intermolecular interaction with the $-PO_3H_2$ of SAM (2PACz) molecule (electronegative P = O group), promoting the uniform distribution and anchoring of SAM on the substrate, ultimately forming a high-quality monolayer. The CTAB endows the SAMs with higher film coverage, better interfacial energy level alignment and promotes perovskite crystallization, improving hole extraction ability and the minimization of voltage loss (V_{loss}). Consequently, the CTAB modified inverted PSCs achieve an enhanced PCE of 26.20% (0.072 cm^2), compared with the control device (23.13%). Moreover, the up-scaled device with an area of 22.96 cm^2 attains an efficiency of 22.34%, proving the scalability of the strategy. The optimized devices maintain > 80% and 90% of the initial PCEs after 800 h at maximum power point tracking (MPPT) and 1000 h at 65 °C, respectively.

Results

Mechanism characterization

Figure 1a illustrates the schematic diagram of CTAB inhibiting 2PACz aggregation, and the structural formulas of 2PACz and CTAB molecules are exhibited in Supplementary Fig. 1. The CTAB addition alleviates 2PACz agglomeration in solution as evidenced by dynamic light scattering (Supplementary Fig. 2). After annealing treatment, 2PACz disperses uniformly on the surface of transparent conductive oxide (TCO) substrate. To eliminate the interference of non-specific or physically adsorbed molecules on the substrate surface, the EDS mapping of P element in 2PACz and 2PACz&CTAB films washed with anhydrous ethanol solvent was analyzed (Supplementary Fig. 3). Compared with 2PACz, there is no significant difference between 2PACz&CTAB before and after washing. This result suggests that CTAB promotes a more uniform distribution of 2PACz on the substrate, thereby minimizing non-specific adsorption or physical adsorption molecules on the substrate surface. To reveal the mechanism of CTAB-mediated agglomeration inhibition and dispersion promotion, density functional theory (DFT) calculation and molecular dynamics (MD)

simulation were carried out on 2PACz (control SAM) and 2PACz&CTAB (target SAM) mixtures. The surface electrostatic potential analysis reveals that the electronegative P = O group of 2PACz interacts with the positively charged N atom of CTAB (Supplementary Fig. 4). The density functional theory (DFT) calculations reveal the adsorption energies of 2PACz molecule and 2PACz&CTAB on SnO_2 substrate are -1.935 eV and -2.817 eV (Supplementary Fig. 5), respectively, while corresponding binding energies are -2.763 eV and -3.491 eV (Fig. 1b), respectively. Compared to pure 2PACz, the 2PACz&CTAB system on FTO substrate exhibits significantly higher adsorption and binding energy, indicating stronger interfacial interaction. This thermodynamic preference drives the preferential adsorption of 2PACz&CTAB on the FTO surface. The Independent Gradient Model (IGM) analysis (Supplementary Fig. 6) quantitatively reveals that CTAB introduction strengthens non-covalent interactions compared with the reference system, as evidenced by the enhanced characteristic blue isosurface (attraction interaction) in the spatial distribution. MD simulations establish the model top view of 2PACz and 2PACz&CTAB on SnO_2 substrate (Fig. 1c and Supplementary Figs. 7 and 8), demonstrating that CTAB doping effectively suppresses 2PACz agglomeration while improving substrate coverage. To further quantify the effect of CTAB on the dispersion of 2PACz on TCO substrate, XPS of O 1s orbitals for bare FTO, FTO/2PACz and FTO/2PACz&CTAB are characterized (Fig. 1d). The peak area of Sn-O-P/Sn-O-H increases from 14.77% to 24.31% when comparing bare FTO with FTO/2PACz and FTO/2PACz/CTAB, indicating enhanced SAM coverage. To more accurately exclude interface molecules arrangement, we analyzed the XPS spectra of the O 1s orbitals of 2PACz samples with different treatments (Supplementary Fig. 9, Supplementary Table 1). The peak area of Sn-O-P/Sn-O-H in pure 2PACz decreases from 22.37% to 13.27% after solvent washing, a reduction of 40.67%. On the contrary, the peak area of Sn-O-P/Sn-O-H in CTAB-optimized 2PACz shows slightly decrease from 29.35% to 25.66% (12.57% reduction), and the peak area is still larger than that of pure 2PACz (22.37%). The plasma etching of perovskite from the buried layer interface confirms that CTAB does not remain within the perovskite (Supplementary Fig. 10). These results prove that CTAB enhances the formation of chemical anchoring between 2PACz and the surface but it is not doped in the perovskite phase, while also minimizing the presence of non-anchored molecules. The target SAM exhibits no additional absorption relative to the relative to the control (Supplementary Fig. 11), while improves the energy level alignment (Supplementary Fig. 12). CTAB introduction increases the distance between SAM molecules. While increasing the coverage of SAM, it destroys or weakens the π - π stacking interaction, leading to further modulation of the SAM work function. Specifically, the target SAM shows a deeper energy level work function (W_f), facilitating more efficient hole extraction and transport between the perovskite layer and transport layer. Moreover, Kelvin Probe Force Microscopy (KPFM) further indicates a higher surface potential and an improved uniformity for the target SAM, implying superior hole transport characteristics (Supplementary Fig. 13).

Characterization of perovskite films

To further evaluate the impact of control (2PACz) and target SAM (2PACz&CTAB) on perovskite film quality, we performed comprehensive film characterization (Fig. 2). X-ray diffraction (XRD) demonstrates the enhanced crystallinity in perovskite film deposited on target SAM, resulting from the uniform dispersion and coverage of target SAM on FTO substrate (Fig. 2a, Supplementary Fig. 14 and Supplementary Table S2). The grazing incidence small angle X-ray scattering (GISAXS) test suggests that the CTAB addition markedly improve the scattering signal intensity along the (110) direction while decrease residual PbI_2 in perovskite films (Fig. 2b and Supplementary Fig. 15), which is consistent with the XRD results. The scanning electron microscope (SEM) images demonstrate that target SAM is more

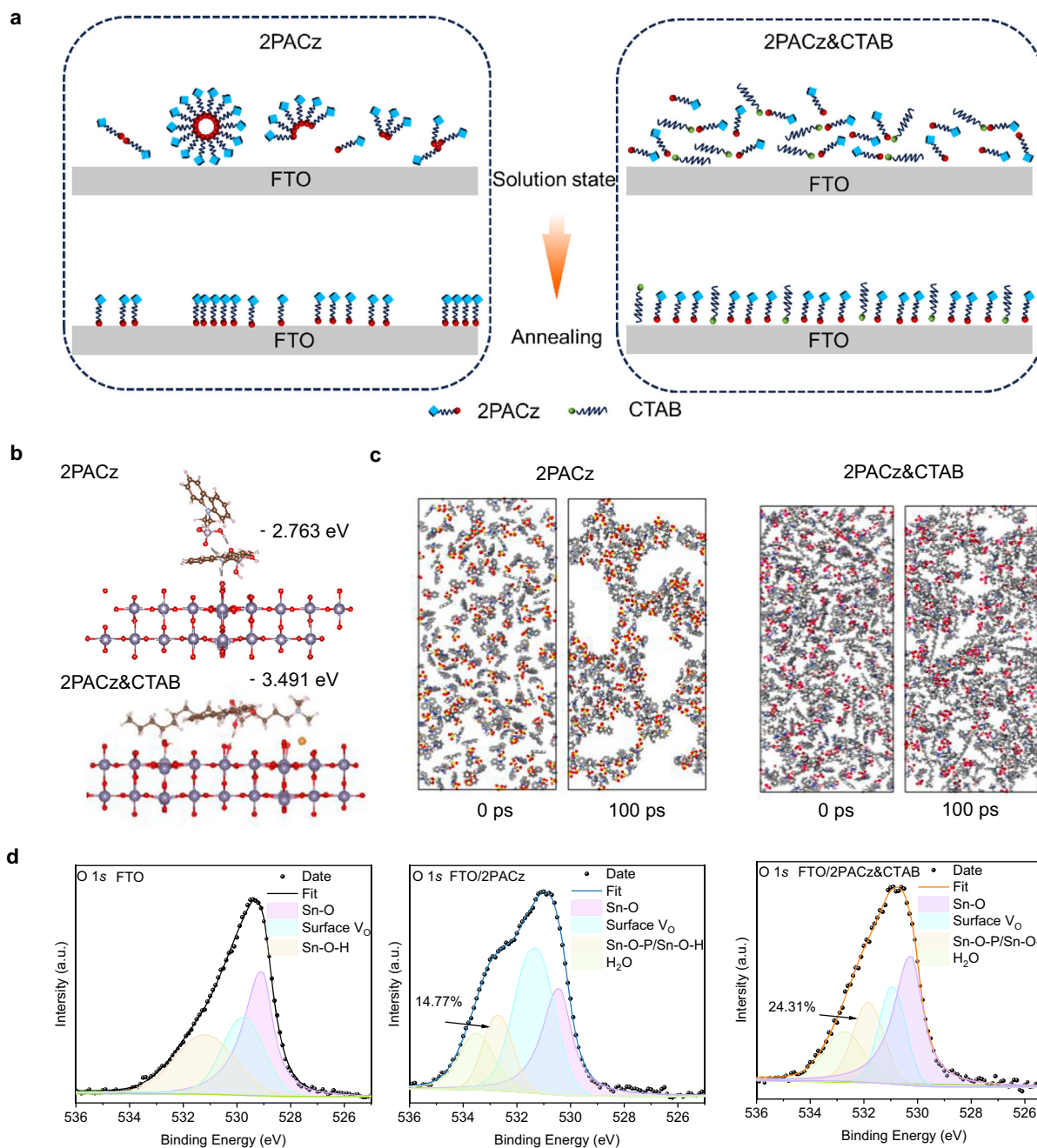


Fig. 1 | Theoretical simulation and experimental characterization of molecules. **a** The schematics of control (2PACz) and target (2PACz&CTAB) SAM. **b** The binding energy model of control and target SAM molecules on SnO₂ substrate calculated by

DFT simulation. **c** Molecular dynamics model of control and target SAM molecules on SnO₂ substrate. **d** XPS spectra of O 1s for the FTO, FTO/2PACz, and FTO/2PACz&CTAB.

conductive to the larger perovskite grains formation and effectively reduces the grain boundaries of the perovskite films (Fig. 2c-d). Statistically grain size analysis further confirms the morphological improvements (Supplementary Fig. 16), attributable to the better coverage, thereby adjusting the nucleation rate to promote high-quality crystallization. After CTAB optimization, the contact angle between 2PACz film and perovskite solution increases from 10° to 15° (Supplementary Fig. 17). According to the wetting function $f(\theta) = \frac{(2 + \cos \theta)(1 - \cos \theta)}{4}$, where the $f(\theta)$ represents the ratio of nucleation work between heterogeneous and homogeneous nucleation, θ denotes the contact angle between the gas-liquid interface and the solid-liquid interface¹⁰, a larger θ corresponds to the higher $f(\theta)$. Therefore, the improved contact angle indicates the heterogeneous nucleation increases and the nucleation difficulty enhances. This

reduces the nucleation sites generation and promotes larger grain size (Supplementary Figs. 18 and 19). The cross-section SEM reveals that the perovskite films on target SAM has lower grain boundary density and surface roughness, facilitating decreased grain boundary defects and promote carrier transport (Fig. 2e). Atomic force microscope (AFM) test quantitatively confirms the roughness reduction, showing a decrease from 14.55 nm to 11.09 nm (Fig. 2f). The results demonstrate that target SAM is more conducive to the perovskite crystallization, yielding larger grains with lower grain boundary defects.

Optical properties of perovskite films

Carrier dynamics of perovskite films with different SAMs were investigated in Fig. 3. The UV-Vis test exhibits there is no bandgap shift between the control and target SAM based perovskite films (Fig. 3a,

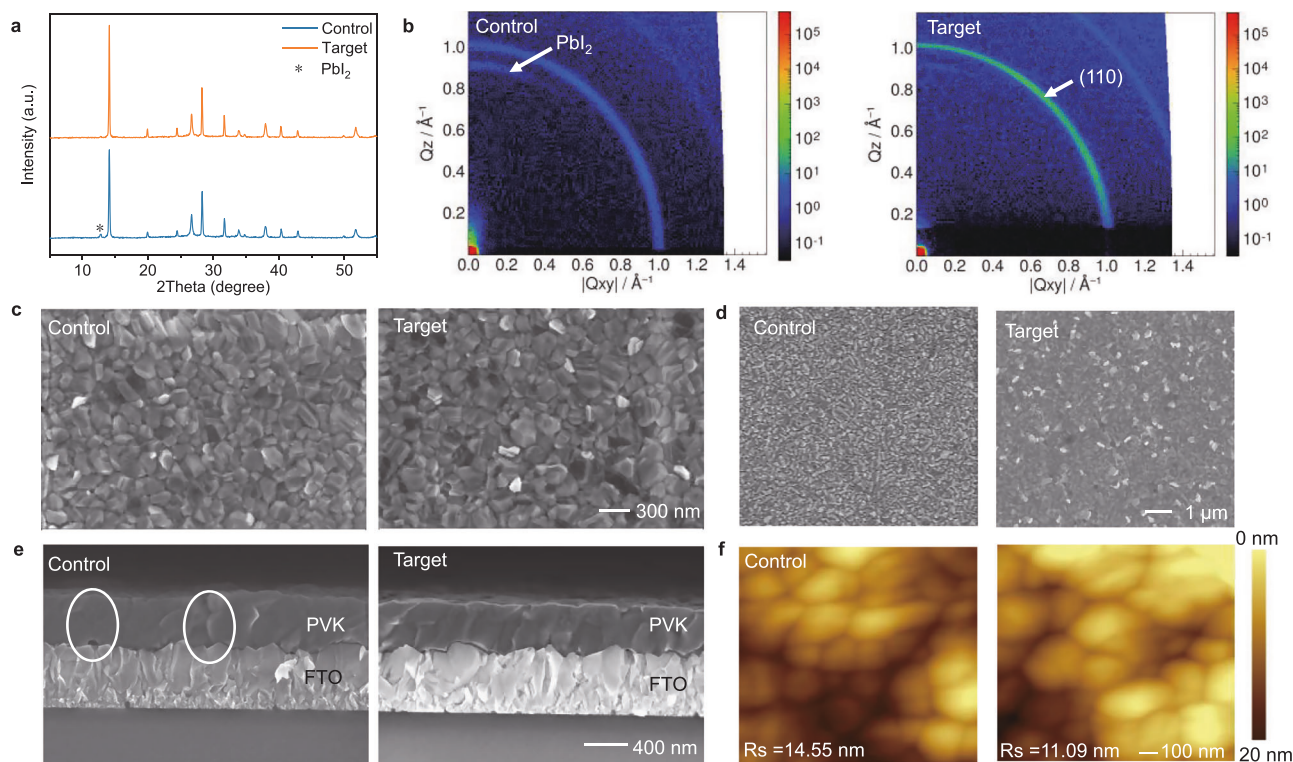


Fig. 2 | Characterizations of perovskite films deposited on SAMs. **a** The XRD patterns, **b** The GISAXS images, **c, d** SEM, **e** The cross-section SEM and **f** AFM images of perovskite films on the control and target SAMs.

Supplementary Fig. 20). In Fig. 3b, c, photoluminescence (PL) and time-resolved fluorescence spectroscopy (TRPL) tests prove enhanced PL signals and prolonged average carrier life of 37.54 ns for target film and 7.34 ns for the control film (Supplementary Table 3), respectively, indicating the reduced defect by the uniform coverage of SAM layer and improved crystallinity of perovskite film. To further verify the effect of target SAM on carrier transport, we tested the PL and TRPL of perovskite films by glass surface excitation (Supplementary Fig. 21, Supplementary Table 4). The PL signals of perovskite films are weaker for the target SAM compared to the control, and the average lifetimes of the perovskite films corresponding to control and target are 24.58 ns and 13.10 ns, respectively. To determine whether CTAB itself can directly extract carriers, we prepared perovskite films based on glass, CTAB, 2PACz, 2PACz&CTAB (PVK, CTAB/PVK, 2PACz/PVK, 2PACz&CTAB/PVK), and tested the PL and TRPL of perovskite films (Supplementary Fig. 22, Supplementary Table 5). CTAB alone enhances the PL signal due to the improved perovskite films, indicating it cannot directly extract carriers. However, the sample of 2PACz/PVK shows reduced PL intensity and carrier lifetime versus bare glass. Critically, 2PACz&CTAB/PVK films exhibit the lowest PL and carrier lifetime among all samples. This demonstrates that CTAB facilitates efficient carrier extraction/transfer not through direct interaction, but by suppressing 2PACz aggregation to improve SAM uniformity and coverage. Transient absorption spectroscopy (TA) was performed to further investigate carrier dynamics. In TA 2D contour map (Fig. 3d-e), the perovskite film based on control and target SAM shows a ground state bleaching peak (GSB) at 780 nm. Usually, GSB signal intensity is positively correlated with carrier density. Notably, the perovskite films with target SAM demonstrate enhanced GSB signals at equivalent delay times (Fig. 3f-g), indicating superior film quality and increased carrier generation efficiency. PL Mapping exhibits the improved luminescence intensity and evenly perovskite films with target SAMs compared with the control films (Fig. 3h-i). The above observations confirm that the uniform coverage SAM layer by CTAB facilitates excellent

crystal quality with reduced grain boundary defects for optimized carrier dynamics.

Photovoltaic performance

To investigate the effect of CTAB-modified SAMs on device performance, we determined the optimal concentration of CTAB based on the structure of glass/FTO/SAM (2PACz or 2PACz&CTAB)/Perovskite/C₆₀/BCP/Ag (Supplementary Fig. 23). The optimal concentration of 2PACz is fixed at 0.5 mg/mL (Supplementary Fig. 24). The same CTAB solution at fixed concentration (0.5 mg/mL) was prepared and mixed with 2PACz solution in varying CTAB:2PACz volume ratios (10%, 30%, 50%, 70% and 100%) by vortex mixing for homogenization. As the proportion of CTAB increases, both device performance and repeatability initially increase and then decline, reaching optimal values at volume ratio of 30% (Supplementary Figs. 25 and 26, Supplementary Table 6). The higher CTAB concentration (>30%) lead to reductions in both J_{SC} and FF, attributing to the fact that CTAB cannot carry out effective transport charges and only promotes 2PACz dispersion. To clarify the effect of residual physically adsorbed molecules on photovoltaic performance, devices with ethanol-washed 2PACz and 2PACz&CTAB layers were compared (Supplementary Fig. 27, Supplementary Table 7). The washed 2PACz devices show slight PCE improvement (from 23.13% to 23.95%), while 2PACz&CTAB devices exhibit a more substantial increase (from 23.13% to 26.20%). Crucially, further cleaning of 2PACz&CTAB layers causes negligible performance changes, confirming minimal non-specific/physical adsorption. This demonstrates that CTAB inhibits solution agglomeration to achieve uniform 2PACz distribution, enabling optimal carrier extraction. The target device achieves a champion PCE of 26.20%, open-circuit voltage (V_{OC}) of 1.17 V, short-circuit current density (J_{SC}) of 25.91 mA/cm², fill factor (FF) of 86.45% (Fig. 4a, Supplementary Fig. 28 and Supplementary Table 7). Besides, the target device exhibits significantly reduced hysteresis compared to the control device (Supplementary Fig. 29). The integrated current densities from the external quantum efficiency

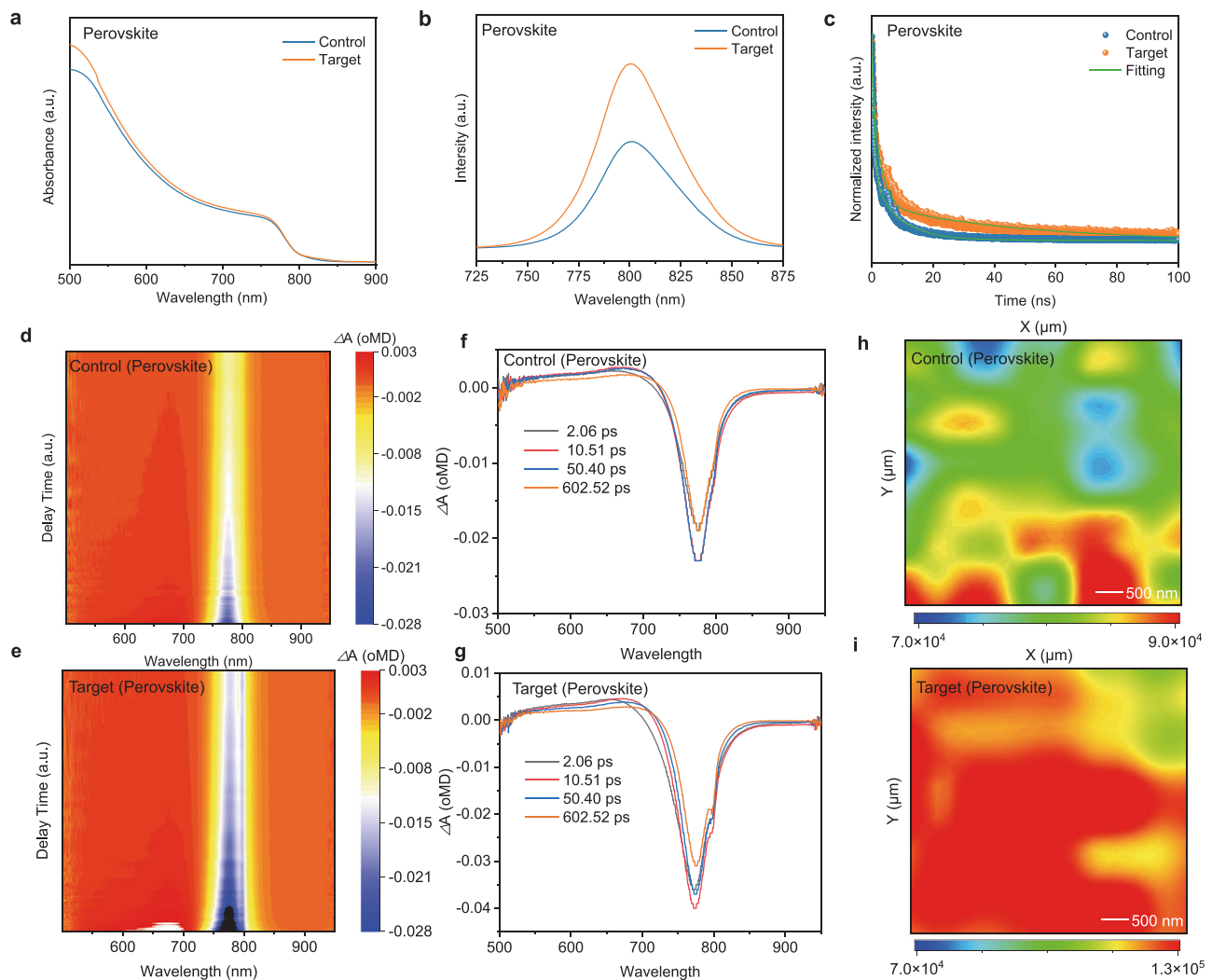


Fig. 3 | Optical characterization of perovskite films deposited on SAMs. **a** The absorption spectra, **b** PL spectra, **c** TRPL spectra of perovskite film on the control and target SAM. **d, e** TA spectra of perovskite films deposited on the control and

target SAM. **f, g** The different delay times TA spectra of perovskite films based on the control and target SAM. **h, i** PL mapping images of the control and target perovskite film.

(EQE) spectra for both the control and target PSCs show close agreement with the J_{SC} values (Fig. 4b). The steady-state output current corresponding to the control and target devices is 23.70 mA/cm² and 24.76 mA/cm², respectively, and the PCE is 22.80% and 25.55% at 0.96 V and 1.02 V (Fig. 4c). The ideal factor (n) derived from the dependence between light intensity and V_{OC} reduces from 1.54 of the control to 1.38 for the target PSCs (Fig. 4d). The lower n closer to 1 indicates the lower defect and non-radiative recombination by CTAB. In addition, the PSCs with target SAM exhibit reduced dark current (Fig. 4e) and increased composite resistance (R_{rec}) (Supplementary Fig. 30), which is attributed to uniform film coverage and improved perovskite film quality. Mott-Schottky curves exhibit a larger built-in potential (V_{bi}) by CTAB, implying more efficient carriers transport (Fig. 4f). Uniform SAM coverage facilitates efficient large-area perovskite solar modules (PSM) on 6 × 6 cm² FTO substrates (Fig. 4g). PSMs with an area of 22.96 cm² obtain the PCEs of 19.55% for control and 22.34% for the target, respectively (Fig. 4h, Supplementary Fig. 31 and Supplementary Table 8). Statistical analysis of 12 devices reveals improved efficiency distribution for the target PSM (Fig. 4i). The stability of the device was also evaluated (Fig. 4j-k). The encapsulated device maintains >80% of its initial PCE after 800 h of maximum power point tracking (MPPT) under ISOS-L-1 conditions (25 °C, 30–40% RH), while the efficiency of the control device retains less than 60% of the initial efficiency after the

same duration. The unencapsulated device maintains >90% initial efficiency following 1000 h of thermal aging at 65 °C in N₂ atmosphere (ISOS-D-2). Whereas the control device keeps only 72% of the initial efficiency. The excellent operational stability originates from the reduced defects via enhanced SAM coverage and improved perovskite crystallization by CTAB.

Discussion

We have introduced a cationic surfactant CTAB in SAM solution to address the inherent aggregation issue of SAMs in p-i-n PSCs. Through simulation and experiments, we prove that the non-self-assembled and non-conductive CTAB can be used as an effective regulator. By leveraging its special electrostatic potential distribution to form non-bonded molecular interaction with 2PACz, CTAB promotes the uniform distribution and anchoring of 2PACz on the substrate. The CTAB-optimized SAM layer promotes perovskite crystallization, manifested as increased grain size, minimized grain boundary defects and suppressed non-radiative recombination. The fabricated device achieves a PCE of 26.20% and an FF as high as 86.45%. Notably, this strategy highlights the scalability, yielding a PCE of 22.34% for the amplifier module (22.96 cm²). The devices exhibit excellent operational stability under ISOS-L-1 and ISOS-D-2 conditions, retaining >80% and >90% of their initial PCEs, respectively. This work provides the critical role of

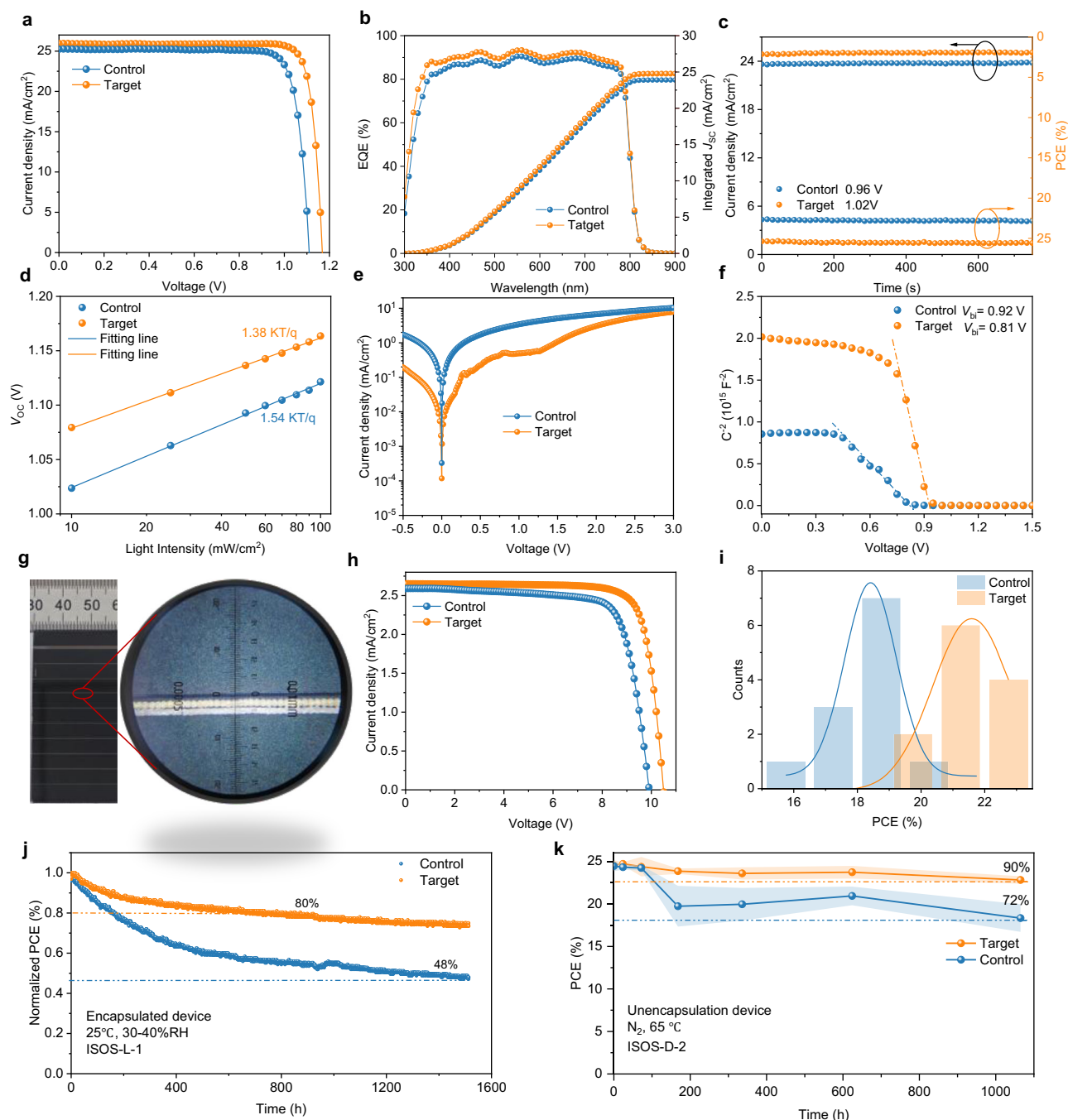


Fig. 4 | The performance and stability of photovoltaic devices. **a** The J - V curves and **b** EQE spectra and integrated J_{sc} of control and target devices. **c** Stable power output curves under MPP conditions. **d** Light intensity dependence, **e** dark J - V curves, **f** Mott-Schottky plots of control and target PSCs. **g** The enlarged picture of

the dead zone. **h** The J - V curves of the control and target PSMs. **i** The efficiency distribution of 12 PSMs based on control and target SAM. **j** The MPPT test of the device under illumination. **k** Devices' stability tested at 65 °C in N₂.

surfactant-assisted molecular dispersion of SAMs in advancing high-performance, large-area perovskite photovoltaics.

Methods

Materials

CsI (cesium iodide), FAI (formamidinium iodide), MABr (Methylammonium bromide), PbI₂ (lead(II) iodide), PbBr₂ (lead(II) bromide), C₆₀ (Fullerene), BCP (Bathocuproine), PEAI (2-Phenylethylamine Hydroiodide) and MACl (methylamine hydrochloride) were purchased from Xi'an Yuri Solar Co., Ltd. FTO were purchased from Suzhou ShangYang Solar Technology Co., Ltd. (2-(9H-carbazol-9-yl)ethyl)

phosphonic acid (2PACz) and cetyltrimethylammonium bromide (CTAB) was purchased from TCI. DMF (dimethylformamide), DMSO (dimethyl sulfoxide) and Chlorobenzene (CB) were purchased from Alfa Aesar. All materials were used as received without further purification.

Preparation of perovskite solution

For Cs_{0.05}(FA_{0.95}MA_{0.05})_{0.95}Pb(I_{0.95}Br_{0.05})₃, the 1.5 M perovskite precursor solution was prepared by mixing FAI, CsI, MABr, PbBr₂, and PbI₂ in a DMF:DMSO (4:1, vol/vol) solvent mixture, with an additional 9 mol % PbI₂ and 15 mol% MACl. For Br-free perovskites, the 1.5 M perovskite

precursor solution was prepared by mixing FAI, CsI and PbI_2 in a DMF:DMSO (4:1, vol/vol) solvent mixture, with an additional 5 mol% PbCl_2 and 5 mol% MACl.

Device fabrication

Fabrication of Perovskite Solar Cells: The patterned FTO (15 Ω/sq) glass was sonicated twice in soapy water, deionized water, and anhydrous ethanol solution for 20 minutes each time, and then placed in an oven for later use. Firstly, the clean FTO substrate was placed in UV-Ozone for 20 min, and then the 0.5 mg/mL of 2PACz or 2PACz/CTAB in ethanol was spin-coated at 5000 rpm for 20 s and annealed at 120 °C for 10 min. For $\text{Cs}_{0.05}(\text{FA}_{0.95}\text{MA}_{0.05})_{0.95}\text{Pb}(\text{I}_{0.95}\text{Br}_{0.05})_3$ perovskite films, the perovskite precursor solution was spin-coated onto the FTO/SAMs layer in a two-step process at a glove box ambient temperature of 20 °C, 2000 rpm for 10 s and 5,000 rpm for 40 s. During the second step, 160 μL of chlorobenzene was dripped on the perovskite film at 12 s before the ending of program. The films were then annealed at 120 °C for 20 min. For modified perovskite films, the PEAI solution in IPA (2 mg/ml) was spin-coated onto the perovskite film at 5000 rpm for 30 s and annealed at 100 °C for 5 min. The final 20 nm C_{60} , 8 nm BCP and 150 nm Ag were deposited via thermal evaporation at a vacuum of 10^{-5} Pa.

Fabrication of Large-Area PSC Modules: For the fabrication of $6 \times 6 \text{ cm}^2$ perovskite modules, fluorine-doped tin oxide (FTO) substrates were first patterned into nine discrete sub-cells via laser etching, with adjacent P1 scribe lines spaced 5.2 mm apart. The etched FTO was ultrasonically cleaned by soap water, ultrapure water and absolute ethanol in turn, and placed in an oven for backup. The 2PACz&CTAB or 2PACz solution was spin-coated at 4000 rpm for 20 s on a glass substrate treated with ultraviolet ozone for 20 min and heated at 100 °C for 10 min. The perovskite precursor solution was deposited by spin-coating at 4000 rpm for 15 s. Then the wet film was rapidly transferred to a custom-built vacuum chamber and exposed to a low-pressure environment (10 Pa) for 5 s. Subsequently, thermal annealing was performed at 100 °C for 30 min in ambient air. Following cooling to room temperature, phenethylammonium iodide (PEAI) solution (2 mg/mL in isopropanol) was spin-coated onto the perovskite layer at 4000 rpm for 30 s. Then, 20 nm C_{60} and 20 nm SnO_2 were prepared by thermal evaporation and atomic layer deposition (ALD), respectively, and the above functional layers were treated with P2 by laser. Finally, 50 nm Ag was prepared by thermal evaporation at 10^{-4} vacuum degree, and then the Ag electrode was treated with P3. Module fabrication proceeded through the following laser patterning sequence: P1 patterning: Laser scribing of FTO with a line width of 40 μm ; P2 patterning: After sequential deposition of the electron transport layer (ETL), perovskite layer, and hole transport layer (HTL), laser scribing with a line width of 60 μm ; P3 patterning: Mechanical scribing (50 μm width) of the Ag back electrode to establish series interconnection.

Characterization of films and devices

X-ray diffraction (XRD) patterns were analysis with Cu K α radiation (D-max 2500 PC, Rigaku Corporation, Japan). The composition and work function of perovskite were measured using the X-ray photoelectron spectroscopy and ultraviolet photoelectron spectroscopy (XPS and UPS, Thermo Scientific EscaLab 250 Xi, USA). The particle size distribution of the SAM solution was measured by a laser particle size analyzer (BeNano 90 Zeta, Bettersize, China). The UV-Vis spectra of perovskite films were measured using the ultraviolet-visible spectrophotometer (CARY 100 UV-Vis, Agilent Technologies, USA). PL (excitation at 520 nm) and TRPL characteristics were obtained using FLS980 (Edinburgh Instruments Ltd.). The morphology and crystallinity of the perovskite films were studied with field-emission scanning electron microscopy (FE-SEM; SUPRA, Zeiss, Germany). The $J-V$ measurements were determined via a Keithley 2400 source and the solar

simulator with standard AM 1.5 G (Newport Oriel 94043 A, Enlitech, SS-X, AM1.5, 100 mW cm^{-2}). PL mapping was achieved with the excitation light source of a continuous wave 375 nm 200 kHz laser. The scanning step length in X and Y directions of $\times 10$ objective lens is 10 μm . Grazing incidence small angle X-ray scattering (GISXAS) is tested using Xenocs equipment, with an incident angle of 0.2°. SEM images were taken on a JEOL JSM-7800. Atomic force microscopy (AFM) and Kelvin Probe Force Microscopy (KPFM) were recorded using a Cypher ES, Oxford Instruments, UK. In addition, all evaporation equipment adopts Wuhan PUDI vacuum equipment.

Theoretical calculation

Molecular Dynamics Simulation Protocol: i) Initial System Construction, a periodic simulation box with dimensions $6.3 \times 13.6 \times 7.3 \text{ nm}^3$ was constructed, containing 140 molecules of species 1 and 140 molecules of species 2. The atomic configurations were initialized using pre-equilibrated structural files. Interatomic interactions were modeled using the all-atom consistent valence force field (CVFF) force field. Short-range van der Waals interactions were computed via the Lennard-Jones potential with a cutoff radius of 13.043 Å, employing geometric mixing rules for cross-term parameter optimization. Long-range Coulombic interactions were treated using the PPPM (Particle-Particle Particle-Mesh) algorithm, with a relative accuracy threshold of 1×10^{-4} to ensure controlled charge distribution errors. Covalent bonding interactions were described by harmonic potentials for bond stretching (bond style harmonic, potential function $U = K(r-r_0)^2$), angle bending (angle style harmonic), and dihedral torsion (dihedral style harmonic). Improper geometries were constrained using the CVFF potential function (improper style cvff). ii) Energy Minimization, the conjugate gradient (CG) algorithm (min style cg) was employed for global energy minimization, with dual convergence criteria set to 1×10^{-15} for both energy and force residuals. The maximum iteration limit was extended to 10^6 steps to ensure thorough relaxation of local energy minima. iii) Thermodynamic Equilibration, the system was equilibrated under the NVT ensemble using a Nose-Hoover thermostat with a temperature coupling constant of 0.1 ps to maintain 298 K. A time step of 1 fs (timestep 0.01) was adopted, and initial atomic velocities were assigned according to the Maxwell-Boltzmann distribution via the velocity command. Molecular dynamics simulations were performed for 10^5 steps (100 ps), with trajectory files (dump. Lammppstrj) recorded every 5 ps. Equilibration was confirmed when total energy fluctuations stabilized within $\pm 3\%$ of the mean value. iv) Data Analysis, post-simulation visualization and structural snapshots were generated using the OVITO software package for atomic-scale resolution analysis. This protocol adheres to standard LAMMPS (Large-scale Atomic/Molecular Massively Parallel Simulator) input syntax and computational methodologies.

Density Functional Theory (DFT): We used the DFT as implemented in the CP2K 2024.3 in all calculations. The exchange-correlation potential is described by using the generalized gradient approximation of Perdew-Burke-Ernzerhof (GGA-PBE). Grimme's DFT-D3 with (Beck-Johnson) BJ factor was used to describe the dispersion interactions among all the atoms in adsorption models. The convergence criteria of 5.0×10^{-6} for electron step, max atomic force of 4.5×10^{-4} , max geometry change of 3×10^{-3} were set to ensure that structures are fully optimized and the electron wave function had converted to a stable state. The DZVP-MOLOPT-SR-GTH and TZV2P-MOLOPT-SR-GTH were used during optimization and single point calculation, respectively. The opted structures and NCI are visualized by VESTA and VMD, respectively. All wavefunction analysis was carried out on Multiwfn 3.8 Dev.

Reporting summary

Further information on research design is available in the Nature Portfolio Reporting Summary linked to this article.

Data availability

All data generated or analyzed during this study are included in the published article and its Supplementary Information. Additional data are available from the corresponding author on request. Source data are provided with this paper.

References

1. Li, D. et al. Co-adsorbed self-assembled monolayer enables high-performance perovskite and organic solar cells. *Nat. Commun.* **15**, 1–13 (2024).
2. Park, S. M. et al. Low-loss contacts on textured substrates for inverted perovskite solar cells. *Nature* **624**, 289–294 (2023).
3. Qu, G. et al. Conjugated linker-boosted self-assembled monolayer molecule for inverted solar cells. *Joule* **8**, 2123–2134 (2024).
4. Tang, H. et al. Reinforcing self-assembly of hole transport molecules for stable inverted perovskite solar cells. *Science* **383**, 1236–1240 (2024).
5. Tao, M. et al. Molecule-triggered strain regulation and interfacial passivation for efficient inverted perovskite solar cells. *Joule* **8**, 3142–3152 (2024).
6. Wang, A. et al. High-efficiency Sn-Pb perovskite solar cells via nucleation and crystallization control. *Adv. Mater.* **73**, 2418766 (2025).
7. Wang, A. et al. Ionic liquid reducing energy loss and stabilizing cspbi₂br solar cells. *Nano Energy* **81**, 105631–40 (2021).
8. Wang, A. et al. Halogenated hole selective contact enhances interfacial weak bonding of perovskite solar cells. *Adv. Energy Mater.* **14**, 2400641–2400648 (2024).
9. Wu, J. et al. Bisphosphonate-anchored self-assembled molecules with larger dipole moments for efficient inverted perovskite solar cells with excellent stability. *Adv. Mater.* **36**, 2401537–44 (2024).
10. Peng, C. et al. Reinforcement of carbazole-based self-assembled monolayers in inverted perovskite solar cells. *ACS Appl. Mater. Interfaces* **17**, 10745–10754 (2025).
11. Pininti, A. R. et al. Resolving scaling issues in self-assembled monolayer-based perovskite solar modules via additive engineering. *Adv. Energy Mater.* **40**, 2403530 (2024).
12. Qu, S. et al. Redox mediator-modified self-assembled monolayer stabilizes a buried interface in efficient inverted perovskite solar cells. *Energy Environ. Sci.* **18**, 3186–3195 (2025).
13. Sun, A. et al. High open-circuit voltage (1.197 V) in large-area (1 cm²) inverted perovskite solar cell via interface planarization and highly polar self-assembled monolayer. *Adv. Energy Mater.* **14**, 2303941–53 (2024).
14. Zhao, Y. et al. Post-assembled alkylphosphonic acids for efficient and stable inverted perovskite solar cells. *Adv. Funct. Mater.* **34**, 240646–240652 (2024).
15. Zhao, J. et al. Performance amelioration of spray-coated perovskite solar cells utilizing a self-assembled monolayer. *ACS Appl. Energy Mater.* **7**, 3540–3549 (2024).
16. Yeo, D. et al. Self-assembled monolayer-based hole-transporting materials for perovskite solar cells. *Nanomaterials* **14**, 175–194 (2024).
17. Xu, H. et al. Constructing robust heterointerfaces for carrier viaduct via interfacial molecular bridges enables efficient and stable inverted perovskite solar cells. *Energy Environ. Sci.* **16**, 5792–5804 (2023).
18. Xiao, J. et al. Functionalized nickel oxide as a hole transport layer for organic solar cells with simultaneous enhancement of efficiency and stability. *J. Mater. Chem. C.* **12**, 5623–5630 (2024).
19. Kim, G. et al. Enhancing surface modification and carrier extraction in inverted perovskite solar cells via self-assembled monolayers. *Nanomaterials* **14**, 0214–0224 (2024).
20. Jiang, W. et al. Spin-coated and vacuum-processed hole-extracting self-assembled multilayers with h-aggregation for high-performance inverted perovskite solar cells. *Angew. Chem. Int. Ed.* **63**, 11731–11740 (2024).
21. Dai, Z. et al. Connecting interfacial mechanical adhesion, efficiency, and operational stability in high performance inverted perovskite solar cells. *ACS Energy Lett.* **9**, 1880–1887 (2024).
22. Cao, Q. et al. Co-self-assembled monolayers modified NiO_x for stable inverted perovskite solar cells. *Adv. Mater.* **36**, 2311970–9 (2024).
23. Shi, C. Y. et al. Modulating competitive adsorption of hybrid self-assembled molecules for efficient wide-bandgap perovskite solar cells and tandems. *Nat. Commun.* **16**, 1–16 (2025).
24. Liu, S. W. et al. Buried interface molecular hybrid for inverted perovskite solar cells. *Nature* **632**, 536–542 (2024).
25. Zhang, Z. Y. et al. Synergistic improvement of structural ordering and interface binding of hole transport monolayer for efficient inverted perovskite solar cells. *Adv. Energy Mater.* **15**, 2500572–84 (2025).
26. Azam, M. et al. Dual functionality of charge extraction and interface passivation by self-assembled monolayers in perovskite solar cells. *Energy Environ. Sci.* **17**, 6974–7016 (2024).
27. Sun, L. et al. Enhanced performance and stability of perovskite solar cells through modification of SnO₂ electron transport layer with stable conformation surfactant. *Adv. Energy Mater.* **92**, 2405581 (2025).

Acknowledgements

K.D. acknowledges the financial support from the Jiangsu Province Postgraduate Research Innovation Plan in 2025 (KYCX25_3921). H.Z. acknowledges the financial support from the Jiangsu Province Postgraduate Research Innovation Plan in 2025 (KYCX25_3941). A.W. acknowledges the financial support from the National Natural Science Foundation of China (52303383), National Key R&D Program of China (2025YFF0516700) and the China Postdoctoral Science Foundation (2024M762713). J.D. acknowledges the Special Fund for Science and Technology Innovation of Jiangsu Province (Grants No. BE2022610). G.L. acknowledges the funding support from the National Natural Science Foundation of China (52503336) and Basic Research Program of Jiangsu (BK20251292). M.K. Nazeeruddin and G. Li acknowledge the support from Southeast University.

Author contributions

K.D. and A.W. conceived and designed the research. K.D., H.Z. and C.H. carried out the fabrication and major characterization of PSCs. K.D., H.Z. and J.D. conducted theoretical simulations. L.L., X.D. and L.Z. contributed for drawing the schematic diagrams. M.N., G.L. and J.D. contributed to the analysis and provided advice. K.D., A.W. and J.D. wrote the initial draft, and all authors contributed to the final paper.

Competing interests

The authors declare no competing interests.

Additional information

Supplementary information The online version contains supplementary material available at <https://doi.org/10.1038/s41467-025-68207-0>.

Correspondence and requests for materials should be addressed to Aili Wang, Lvzhou Li, Mohammad Khaja Nazeeruddin, Guixiang Li or Jianning Ding.

Peer review information *Nature Communications* thanks the anonymous reviewer(s) for their contribution to the peer review of this work. A peer review file is available.

Reprints and permissions information is available at <http://www.nature.com/reprints>

Publisher's note Springer Nature remains neutral with regard to jurisdictional claims in published maps and institutional affiliations.

Open Access This article is licensed under a Creative Commons Attribution-NonCommercial-NoDerivatives 4.0 International License, which permits any non-commercial use, sharing, distribution and reproduction in any medium or format, as long as you give appropriate credit to the original author(s) and the source, provide a link to the Creative Commons licence, and indicate if you modified the licensed material. You do not have permission under this licence to share adapted material derived from this article or parts of it. The images or other third party material in this article are included in the article's Creative Commons licence, unless indicated otherwise in a credit line to the material. If material is not included in the article's Creative Commons licence and your intended use is not permitted by statutory regulation or exceeds the permitted use, you will need to obtain permission directly from the copyright holder. To view a copy of this licence, visit <http://creativecommons.org/licenses/by-nc-nd/4.0/>.

© The Author(s) 2026